Journal of Multidisciplinary Engineering Science and Technology (JMEST)
ISSN: 2458-9403
Vol. 11 Issue 3, March - 2024

Fabrication of TiZrNbMo refractory high-entropy alloys by plasma rotating electrode process and selective laser melting

Zixuan Wu, Hong Huang, Song Li
Powder Metallurgy Research Institute, Central South University, Changsha 410083, China
E-mail address: ls2011sl@csu.edu.cn

***Abstract*—The TiZrNbMo refractory high-entropy alloy (HEA) powders were successfully prepared by plasma rotating electrode process (PREP). Owing to rapid cooling rate and the immiscibility between Zr and Mo, The as-obtained alloy powders show a dendrite structure involving two body-centered cubic (BCC) phases and nearly-spherical shapes with relatively smooth surfaces. Bulk TiZrNbMo HEAs were fabricated by selective laser melting (SLM） using the PREPed powders. The effects of the laser power and scanning rate on the surface morphology, microstructure and microhardness of the as-built HEAs were investigated in details.**

Keywords—Refractory high-entropy alloy; Plasma rotating electrode process; Microstructure; Selective laser melting; Microhardness

I. INTRODUCTION

Based upon the design concept of high entropy alloy (HEA), refractory HEAs composed mainly of high-melting-point elements have gained more attention due to their advantages such as high strength, excellent corrosion, wear and high-temperature oxidation resistances, which shows great potential as high-temperature structural materials [1-3]. However, preparing refractory HEAs is still challenging owing to the high melting points of constituent elements and significant difference among them [4-6]. Currently, most of refractory HEAs are prepared by vacuum arc melting. This method easily leads to heterogeneous microstructure due to elemental segregation and shrinkage porosity when preparing large blocks [7, 8]. Compared with vacuum arc melting, selective laser melting (SLM) method offer some advantages in the fabrication of refractory HEAs such as high energy density laser input suitable for processing refractory metals and reliable ability of obtaining the parts with complex shapes [9-15]. The microstructure and properties of refractory HEA parts prepared by SLM strongly depend on the quality of raw powders. Mechanical alloying, gas atomization, Plasma spheroidization and plasma rotating electrode process (PREP) can be applied for the fabrication of HEA powders. Compared with the first three methods, PREP is more suitable for the preparation of refractory HEA powder used for SLM since it is a cost-effective technique to obtain the powders with high sphericity and low porosity [16-17].

In this work, the TiZrNbMo refractory HEA powders were prepared by PREP and then used as feedstock powders for the subsequent SLM. The surface morphology and compositional homogeneity of the as-received alloy powders were investigated in details. The surface morphology, microstructure and microhardness of the as-built refractory HEA by SLM were also explored.

II. EXPERIMENTAL PROCEDURES

The TiZrNbMo HEA rods with a diameter of 60 mm required for the subsequent PREP are prepared by vacuum electromagnetic levitation melting, and the raw materials used are pure metals with a purity of 99.95% or more. The rod used as the consumable electrode was atomized into the powders by PREP under high-purity Ar atmosphere (Easy gold new materials technology Co, Ltd, China) and the particle size of the powder falls between 15 μm and 53 μm as much as possible by adjusting the feed speed, rotation speed and electron gun power. Bulk TiZrNbMo refractory HEAs with a dimension of 6×6×3 mm were fabricated by using DiMetal-150 laser powder bed melting system (Leijia Co, Ltd, China). The build platform using TC4 substrate, the monolayer thickness is 40 μm, the scanning distance is 80 μm, and the laser scanning angle between the adjacent layers is 69°. The effects of

the laser power and scanning rate on the HEAs obtained by SLM were investigated. The processing parameters are listed in Table 1. The volumetric energy density (VED) is determined according to the formula [18].

Table 1 Processing Parameters of SLM process

No	Scanning rate (mm/s)	Laser power (W)	VED (J*mm^{-3})
0	350	200	179
1-1	350	175	156
1-2	350	180	161
1-3	350	190	170
1-4	350	210	188
1-5	350	220	196
1-6	350	225	201
2-1	200	200	312
2-2	300	200	208
2-3	325	200	192
2-4	330	200	189
2-5	340	200	184
2 6	360	200	174
2-7	370	200	169
2-8	375	200	167
2-9	400	200	156
2-10	450	200	139

Phase constitution of TiZrNbMo HEAs was characterized by D/max2550pc X-ray diffraction (XRD, Cu Kα radiation). Microstructural observation was performed using optical microscopy (OM, Leica DM2700M) and scanning electron microscopy (SEM, TESCAN MIRA4 LMH) equipped with an energy dispersive X-ray (EDX) analysis system (Ultim Max 40). Electron back-scattered diffraction (EBSD) measurement was carried out by a ZEISS EVO MA10 scanning electron microscope (SEM) equipped with the Nordlys Max2 EBSD system. The nanoindentation measurement was performed on a UNHT+MCT nanoindentation tester at the load of 20 mN. The average values of microhardness and elastic modulus were determined according to the values of five spots. The loading rate and unloading rate are both 40 mN/min, and the holding time is 10 s.

III. Results and Discussion

The XRD patterns of the as-received TiZrNbMo HEA ingot and powders as well as bulk specimen obtained by SLM are shown in Fig. 1. For the TiZrNbMo HEA ingots and SLMed specimen, only one set of diffraction peaks corresponding to a single body-centered cubic (BCC) solid solution phase can be found, consistent with our previous work [19]. The diffraction peaks of the PREPed HEA powders are different from those of the other alloys, which indicate the splitting characteristics. This suggests that two BCC phases occur in the PREPed HEA powders owing to the distinct difference in atomic radii and melting points of the constituent elements as well as rapid cooling rate.

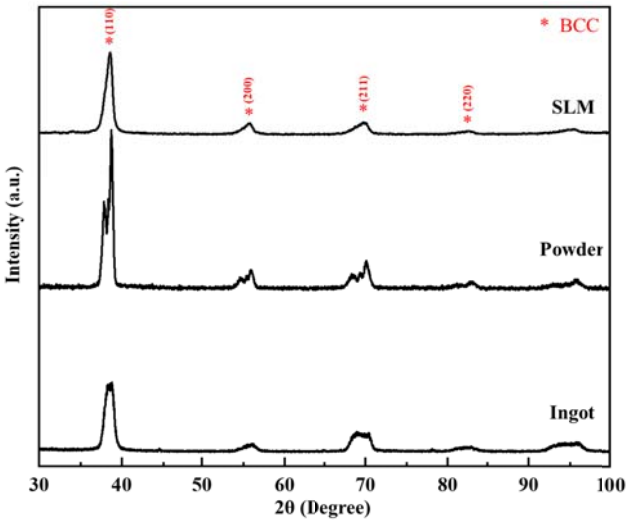

Figure 1 XRD patterns of the as-received TiZrNbMo HEA ingot and powders as well as bulk specimen obtained by SLM

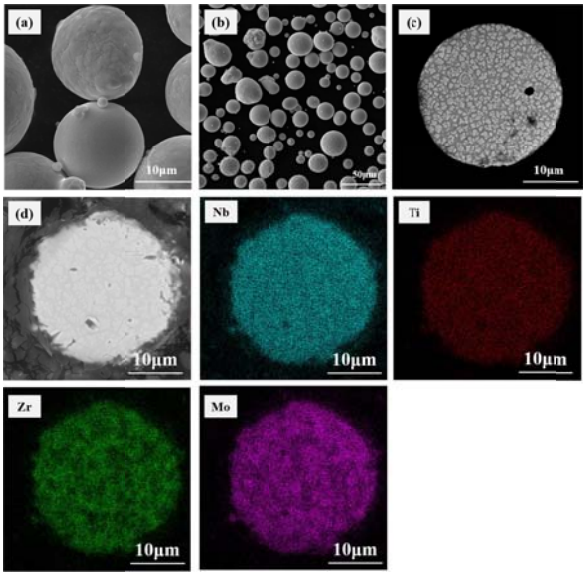

Figure 2 SEM images of the surface and cross section of the PREPed HEA powders: (a) and (b) surface morphology; (c) cross section; (d) polished surface and elemental distribution maps

Figure 2(a) and (b) shows the surface morphology of the PREPed TiZrNbMo HEA powders. It can be seen that the powders exhibit nearly spherical in shape. Otherwise, a small amount of irregular and satellite particles, which are typically several

microns in size, are adhered to the larger particles due to compositional heterogeneity and the collisions of the solidifying droplets. The SEM image of cross- section of the PREPed TiZrNbMo HEA powders shown in Fig. 2(c) confirms that a typical dendrite structure is formed. The elemental distribution scanning (EDS) maps are shown in Fig. 2(d). It can be found that the distribution of Ti and Nb elements are relatively uniform in dendrite and inter-dendrite regions, while Zr and Mo exhibit the opposite distribution tendency, Mo segregates in dendrite region and Zr is rich in inter-dendrite region. The inhomogeneous distributions of Zr and Mo elements are ascribed to the immiscibility between them.

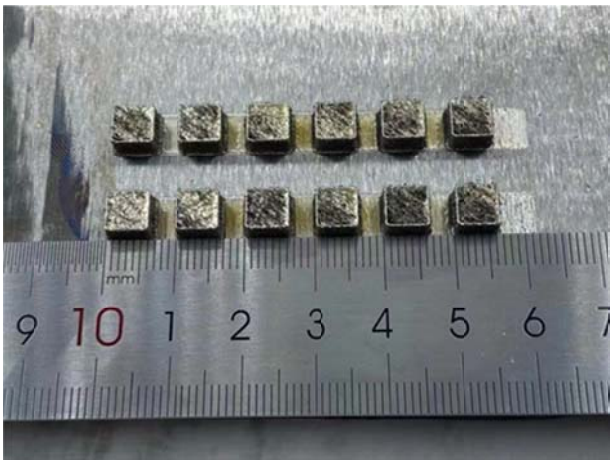

Figure 3 Appearances of the as-built TiZrNbMo HEAs obtained by SLM

The appearances of the as-built TiZrNbMo HEAs obtained by SLM are shown in Fig. 3. After SLM, there is no distinct deformation, delamination and warping on the surfaces of all the as-built specimens, but visible cracks and pores occur on the surfaces of some specimens. The effects of the laser power and scanning rate on the microstructure of the as-built TiZrNbMo HEAs by SLM were systematically investigated. Figure 4 shows the OM images of cross-section of the as-built TiZrNbMo HEAs obtained by SLM at a scanning rate of 350 mm/s. It can be seen that there are many longitudinal thermal cracks and pores on the specimens, but the microstructural defects of Sample 0 are relatively minimal (Fig. 4(d)). When the laser power is 175 W, in addition to the obvious transverse cracks, the longitudinal cracks can also be observed. As the laser power further increases (no more than 200 W), the cracks gradually become thinner and narrower, and the number of cracks and holes also decreases. When the laser power increases to 225 W, the obvious transverse and longitudinal cracks as well as irregular holes with larger sizes can be seen again due to the formation of deep and narrow molten pool during SLM. Figure 5 shows the OM images of cross-section of the as-built TiZrNbMo HEAs obtained by SLM at a laser power of 200 W. Whether the scanning rate is less than or more than 350 mm/s, the obvious transverse and longitudinal cracks also appear, and the crack depth and the number of cracks is larger. When the scanning rate is too high (450 mm/s), there are large areas of holes and the brittleness of the specimen obviously increases. It can be found from Fig. 4 and Fig. 5 that, when the laser power is 200 W and the scanning rate is 350 mm/s, the formability of the specimen (Sample 0) is relatively better, with minimal cracks and pores.

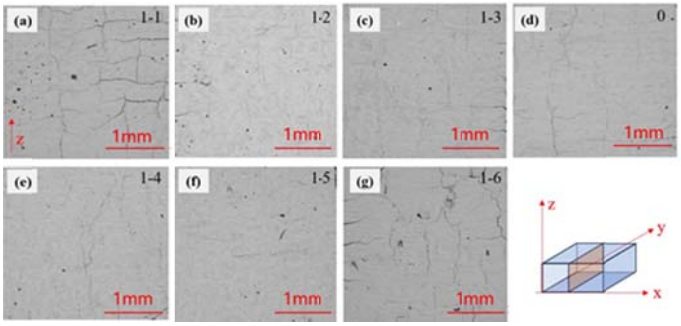

Figure 4 OM images of cross-section of the as-built TiZrNbMo HEAs obtained by SLM at a scanning rate of 350 mm/s: (a) 175 W; (b) 180 W; (c) 190 W; (d) 200 W; (e) 210 W; (f) 220 W; (g) 225 W

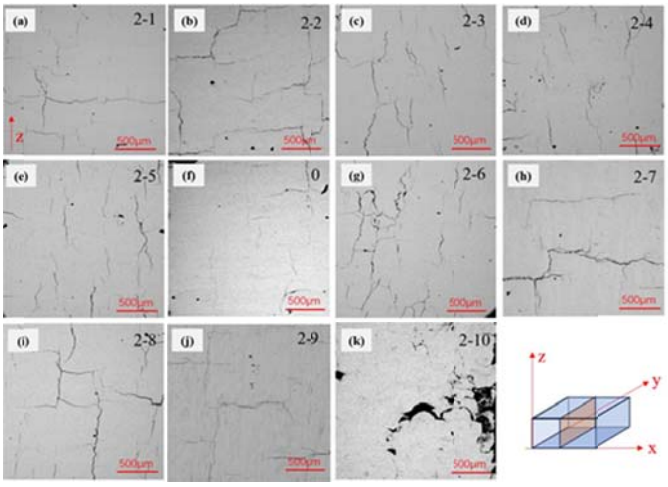

Figure 5 OM images of cross-section of the as-built TiZrNbMo HEAs obtained by SLM at a laser power of 200 W: (a) 200 mm/s; (b) 300 mm/s; (c) 325 mm/s; (d) 330 mm/s; (e) 340 mm/s; (f) 350 mm/s; (g) 360 mm/s; (h) 370 mm/s; (i) 375 mm/s; (j) 400 mm/s; (k) 450 mm/s

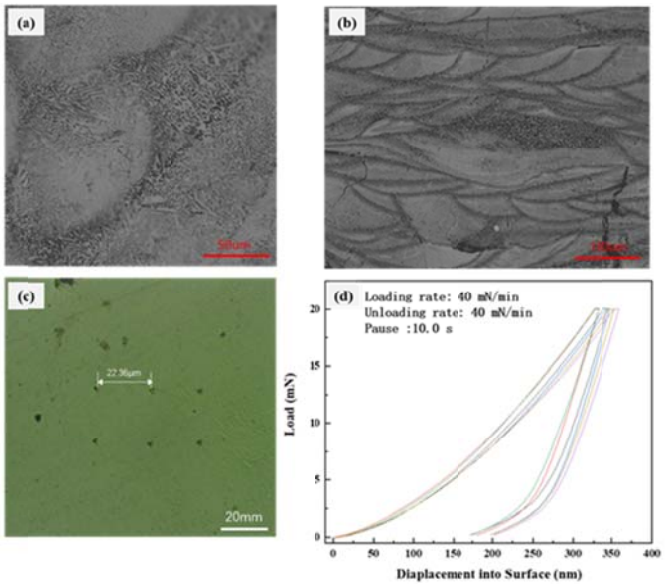

Figure 6 (a) and (b) SEM images of cross-section of the as-built TiZrNbMo HEAs obtained by SLM at a laser power of 200 W and a scanning rate of 350 mm/s; (c) and (d) OM image of the nanoindentation locations and corresponding load-displacement curves

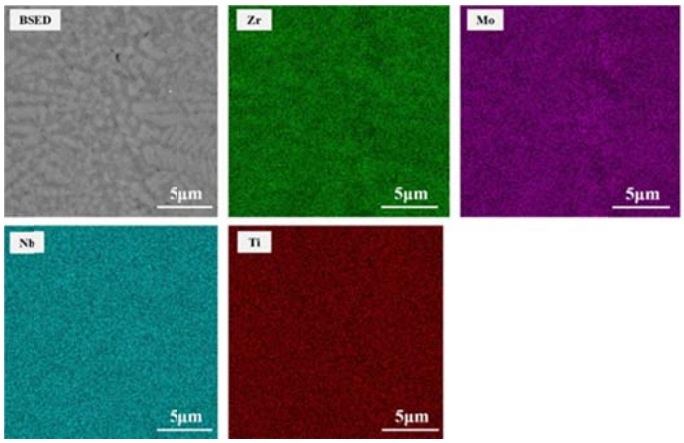

Figure 7 high-magnification backscattered SEM image and corresponding EDS map of the SLMed TiZrNbMo HEA at a laser power of 200 W and a scanning rate of 350 mm/s

To further investigate the microstructure of the SLMed TiZrNbMo HEA, the side surface of Sample 0 is further enlarged and observed by SEM, as shown in Fig. 6(a) and (b). The typical dendrite structure with fine grains and the fish-scale molten pools in a stacked state can be found. The dendrites grow across the boundary of molten pool. Figure 6 (c) and (d) present the OM image of the nanoindentation locations and corresponding load-displacement curves of the SLMed TiZrNbMo HEA (Sample 0). According to the Oliver-pharr method, the hardness (H) and elastic modulus (E) values are determined to be 7.82±0.6 GPa and 151±5.35 GPa, respectively. The high-magnification backscattered SEM image and corresponding EDS map of the SLMed TiZrNbMo HEA (Sample 0) are shown in Fig. 7. After SLM, the dendrite structure is still preserved, similar to the PREPed alloy powders. The segregation of Zr and Mo is slight, but not as severe as that in the PREPed alloy powders. Ti and Zr elements are uniformly distributed.

IV. Conclusion

The pre-alloyed TiZrNbMo nearly-spherical powders were successfully fabricated by PREP. The as-received powders possess a dendrite structure containing two BCC phases due to rapid cooling rate and the immiscibility between Zr and Mo. Bulk TiZrNbMo refractory HEAs was obtained by SLM using the PREPed powders with the particle size between 15 μm and 53 μm, which exhibit a single BCC structure with relatively uniform element distribution. It was difficult to prepare bulk crack- and pore-free TiZrNbMo HEAs by SLM based on the current processing parameters. When the scanning speed is 350mm/s and the laser power is 200W, the formability of the SLMed HEA is relatively better, with less cracks and fine pores. Its microhardness and elastic modulus are 7.82±0.60 GPa and 151.30±5.35 GPa, respectively.

Acknowledgment

This work was primarily financial supported by State Key Laboratory for Powder Metallurgy, Central South University.

References

[1] J. W. Yeh, S. K. Chen, S. J. Lin, J. Y. Gan, T. S. Chin, T. T. Shun, C. H. Tsau, S. Y. Chang, Adv. Eng. Mater., 2004, 6, 299-303.
[2] Y. Zhang, T. T. Zuo, Z. Tang, M. C. Gao, K. A. Dahmen, P. K. Liaw, Z. P. Lu, Prog. Mater. Sci., 2014, 61, 1-93..
[3] J. Chen, X. Zhou, W. Wang, B. Liu, Y. Lv, W. Yang, D. Xu, Y. Liu, J. Alloy. Compd., 2018, 760, 15-30.
[4] O.N. Senkov, S.L. Semiatin, J. Alloys Compd., 2015, 649, 1110-1123.
[5] P. F. Gu, T. B. Qi, L. Chen, T. Ge, X. D. Ren, Int. J. Refract. Met. H., 2022, 105, 105834.
[6] B. G. Zhang, Y. P. Huang, Z. Y. Dou, J. Wang, Z. F. Huang, J. Sci-adv. Mater. Dev., 2024, 9, 100688.
[7] K. G. Pradeep, N. Wanderka, P. Choi, J. Banhart, B.S. Murty, D. Raabe, Acta Mater., 2013, 61, 4696-4706.
[8] C. C. Yang, J. H. Chau, C. J. Weng, C. S. Chen, Y. H. Chou, Mater. Chem. Phys. 2017, 202, 151-158.

[9] M. Sun, B. W. Wang, J. X. Zhang, B. H. Lu, Intermetallics, 2023, 156, 107866.

[10] M. Song, B. W. Ma , H. Q. Huang, L. X. Liu, R. Guo, Y. Z. Yin, H. T. Wang, D. D. Li, N. Li, J. Pan, L. Liu, Mater. Des., 2024, 239, 112754.

[11] H. Z. Tang, R. D. Li, F. Wang, S. Q. Lin, T. C. Yuan, Mater. Charact., 2024. 209, 113679.

[12] Y. Kok, X. P. Tan, P. Wang, M. L. S. Nai, N. H. Loh, E. Liu, S. B. Tor, Mater. Des., 2018, 139, 565-586.

[13] Z. Zhu, Q. Nguyen, F. Ng, X. An, X. Liao, P. Liaw, S. Nai, J. Wei, Scripta Mater., 2018, 154, 20-24.

[14] Y. Chew, G. Bi, Z. Zhu, F. Ng, F. Weng, S. Liu, S. Nai, B. Lee, Mater. Sci. Eng. A, 2019, 744, 137-144.

[15] D. Faidel, D. Jonas, G. Natour, W. Behr, Addit. Manuf., 2015, 8, 88-94.

[16] W. Yang, M. Li, S. Su, S. Xiao, Y. Chen, J. Mater. Res. Technol., 2023, 27, 5204-5218.

[17] Y. Cui, Y. Zhao, H. Numata, K. Yamanaka, H. Bian, K. Aoyagi, A. Chiba, Powder. Technol., 2021, 393, 301-311.

[18] Y. Brif, M. Thomas, I. Todd, Scr. Mater., 2015, 99, 93-96.

[19] L. P. Huang, M. H. Long, W. S. Liu, S. Li, Mater. Lett., 2021, 293, 129718.